





Article

Effect of the Degree of Inversion on the Photoelectrochemical Activity of Spinel ZnFe_2O_4

Luis I. Granone ^{1,2,*}, Konstantin Nikitin ³, Alexei Emeline ³, Ralf Dillert ^{1,2,*} and Detlef W. Bahnemann ^{1,2,3}

¹ Institute of Technical Chemistry, Gottfried Wilhelm Leibniz University Hannover, Callinstrasse 3, D-30167 Hannover, Germany; bahnmann@iftc.uni-hannover.de

² Laboratory of Nano- and Quantum-Engineering (LNQE), Gottfried Wilhelm Leibniz University Hannover, Schneiderberg 39, D-30167 Hannover, Germany

³ Laboratory "Photoactive Nanocomposite Materials", Saint-Petersburg State University, Ulyanovskaya str. 1, 198504 Peterhof, Saint-Petersburg, Russia; konstantin.nikitin@spbu.ru (K.N.); alexei.emeline@spbu.ru (A.E.)

* Correspondence: granone@iftc.uni-hannover.de (L.G.); dillert@iftc.uni-hannover.de (R.D.); Tel.: +49-511-762-16039 (R.D.)

Received: 7 April 2019; Accepted: 7 May 2019; Published: 9 May 2019



Abstract: Physicochemical properties of spinel ZnFe_2O_4 (ZFO) are known to be strongly affected by the distribution of the cations within the oxygen lattice. In this work, the correlation between the degree of inversion, the electronic transitions, the work function, and the photoelectrochemical activity of ZFO was investigated. By room-temperature photoluminescence measurements, three electronic transitions at approximately 625, 547, and 464 nm (1.98, 2.27, and 2.67 eV, respectively) were observed for the samples with different cation distributions. The transitions at 625 and 547 nm were assigned to near-band-edge electron-hole recombination processes involving $\text{O}^{2-} 2p$ and $\text{Fe}^{3+} 3d$ levels. The transition at 464 nm, which has a longer lifetime, was assigned to the relaxation of the excited states produced after electron excitations from $\text{O}^{2-} 2p$ to $\text{Zn}^{2+} 4s$ levels. Thus, under illumination with wavelengths shorter than 464 nm, electron-hole pairs are produced in ZFO by two apparently independent mechanisms. Furthermore, the charge carriers generated by the $\text{O}^{2-} 2p$ to $\text{Zn}^{2+} 4s$ electronic transition at 464 nm were found to have a higher incident photon-to-current efficiency than the ones generated by the $\text{O}^{2-} 2p$ to $\text{Fe}^{3+} 3d$ electronic transition. As the degree of inversion of ZFO increases, the probability of a transition involving the $\text{Zn}^{2+} 4s$ levels increases and the probability of a transition involving the $\text{Fe}^{3+} 3d$ levels decreases. This effect contributes to the increase in the photoelectrochemical efficiency observed for the ZFO photoanodes having a larger cation distribution.

Keywords: ZnFe_2O_4 ; degree of inversion; cation distribution; photoelectrochemical activity

1. Introduction

During the last few years, there has been increasing interest in the study of spinel ZnFe_2O_4 (ZFO) as a photoanode material for photoelectrochemical water oxidation [1–3]. As new scientific investigations in this field are reported, differences concerning the photoelectrochemical activity of ZFO photoanodes prepared by different routes have become evident [4–11]. It is well known that ZFO exhibits a variable structure where the distribution of Zn^{2+} and Fe^{3+} cations between octahedral and tetrahedral sites within the crystal lattice depends on the synthetic conditions [12–18]. Therefore, the reason behind the broad variety of results found in the scientific literature for ZFO photoanodes might be related to the cation distribution. The parameter used to quantify the cation distribution is the degree of inversion, x , which is defined as $[\text{Zn}_{1-x}\text{Fe}_x]^\text{O}[\text{Zn}_x\text{Fe}_{2-x}]^\text{O}_4$ with $0 \leq x \leq 1$ (where

the superscripts T and O denote the tetrahedral and octahedral sites, respectively). When $x = 0$ and $x = 1$, ZFO adopts the so-called normal ($^T[\text{Zn}]^O[\text{Fe}_2]\text{O}_4$) and inverse ($^T[\text{Fe}]^O[\text{ZnFe}]\text{O}_4$) structure, respectively. The degree of inversion of bulk ZFO can be controlled by the calcination of the samples at temperatures higher than 737 K and subsequent quenching [12–15]. Thus, bulk ZFO samples with x ranging from approximately 0.02 to 0.20 can be prepared. Pavese et al. [13] reported degrees of inversion up to $x \approx 0.34$ at 1600 K for bulk ZFO by in situ high-temperature neutron powder diffraction measurements. Nevertheless, as shown by O'Neill [12], degrees of inversion higher than $x \approx 0.20$ cannot be experimentally accessed for bulk ZFO samples prepared by means of a solid-state reaction and subsequent quenching. Calcination temperatures higher than 1200 K are required to increase the degree of inversion above this upper limit and, under these conditions, the rate of re-ordering is too fast to quench the sample. For nanoparticulate ZFO, higher degrees of inversion are likely to be obtained [16–18], and the synthesis of ZFO nanoparticles having an almost completely inverted structure ($x = 0.94$) has been reported [19].

In a recent publication, Zhu et al. [8] reported that the cation distribution in partially reduced ZFO anodes affected the performance of light-induced water oxidation. The authors showed that partially reduced ZFO had a relatively poor crystallinity, but a high degree of inversion exhibited superior photogenerated charge carrier transport when compared to ZFO with a high crystallinity but a low degree of inversion. The research of Zhu et al. pioneered the investigation of the effect of the cation distribution on the photoelectrochemical activity of ZFO. However, a study of the effect of the degree of inversion on the photoelectrochemical activity of pristine ZFO samples exhibiting uniform particle size, crystallinity, and crystallite size is, to the best of our knowledge, missing.

Recently, we reported the preparation of ZFO by a solid-state reaction and its further processing into pellets with varying degrees of inversion [14,20]. The elemental analysis of the ZFO pellets revealed a Fe to Zn ratio of 2:1 within the limit of the experimental error, as expected for ZFO [14]. The absence of non-reacted $\alpha\text{-Fe}_2\text{O}_3$ and ZnO as well as the absence of secondary iron oxide phases, were confirmed by XRD and Raman spectroscopy [14]. Mössbauer spectroscopy confirmed the absence of Fe^{2+} and, hence, of oxygen vacancies for all the ZFO pellets [14]. The crystallite size values deduced from the Rietveld refinements and the particle size distribution obtained from the SEM confirmed that the pellets exhibited similar crystallite and particle sizes independently of the degree of inversion [14,20]. Thus, the degree of inversion was found to be the only independent variable between the different ZFO pellets. These characteristics made it possible to investigate the impact of the degree of inversion on the photoelectrochemical activity of ZFO photoanodes unaffected by other variable parameters such as impurities, the number of oxygen vacancies, the particle size, the crystallite size, and the crystallinity.

In the present work, the photoelectrochemical activity of photoanodes made of pristine ZFO with degrees of inversion increasing from $x \approx 0.07$ to $x \approx 0.20$ is reported. Furthermore, the effect of the cation distribution on electronic properties such as the Fermi level and the electronic structure was investigated for the first time. The electronic structure was studied by means of time-averaged and transient room-temperature photoluminescence spectroscopy. It is well known that the photoluminescence spectrum of a material depends on its particle size, crystallinity, and the presence of point defects [21,22]. Therefore, the crystallinity and crystallite size homogeneity of the synthesized ZFO pellets is of utmost importance in order to access meaningful information concerning the effect of the degree of inversion on the photoluminescence properties. The nature of the observed transitions as well as their lifetime and the impact of the degree of inversion are discussed.

2. Results

ZFO pellets with degrees of inversion of $x \approx 0.07$ (ZFO_773), $x \approx 0.10$ (ZFO_873), $x \approx 0.13$ (ZFO_973), $x \approx 0.16$ (ZFO_1073), and $x \approx 0.20$ (ZFO_1173) were prepared by employing a spinel zinc ferrite synthesized by a solid-state reaction as reported previously [14]. In order to access information concerning the porosity of the ZFO pellets, N_2 and Ar physisorption isotherms were measured. Total pore volumes below $10 \text{ cm}^3 \text{ g}^{-1}$ were obtained for all pellets. These values were at the lower limit of

quantification, suggesting that the samples did not exhibit a considerable porosity. This is an expected result for dense pellets pressed at high pressure. Other consequences of the low porosity were small BET surface areas below $10 \text{ m}^2 \text{ g}^{-1}$. The pellets exhibited values ranging from 3.0 to $9.9 \text{ m}^2 \text{ g}^{-1}$ with an average of $5.3 \text{ m}^2 \text{ g}^{-1}$ and no systematic trend concerning the degree of inversion. Thus, independent of the degree of inversion, negligible total pore volumes and sizes were obtained for the different ZFO pellets.

The photoelectrochemical activity of the photoanodes was evaluated by measuring the photocurrent for the methanol oxidation reaction. Figure 1a shows the current density – voltage (j -V) curves measured under chopped solar simulated light for the ZFO photoanodes with increasing degrees of inversion. The light was turned on and off at 20 s intervals. Onset photocurrents for the methanol oxidation were observed at an anodic bias potential of around $+0.9 \text{ V vs. RHE}$. At a bias potential of $+1.2 \text{ V vs. RHE}$, the dark currents were still negligible and the photocurrents were high enough to allow a direct comparison between the different photoanodes. Figure 1b shows the chopped light chronoamperometry measured at an applied bias of $+1.2 \text{ V vs. RHE}$. It was observed that the photocurrent for the methanol oxidation increased as the degree of inversion rose from $x \approx 0.07$ to $x \approx 0.20$. The photoanodes with degrees of inversion of $x \approx 0.07$, $x \approx 0.10$, and $x \approx 0.13$ showed current densities below $0.05 \mu\text{A cm}^{-2}$. There was a significant increase in the current density from 0.05 to $0.24 \mu\text{A cm}^{-2}$ as the degree of inversion increased from $x \approx 0.13$ to $x \approx 0.16$. The current density further increased up to $0.77 \mu\text{A cm}^{-2}$ as the degree of inversion increased from $x \approx 0.16$ to $x \approx 0.20$.

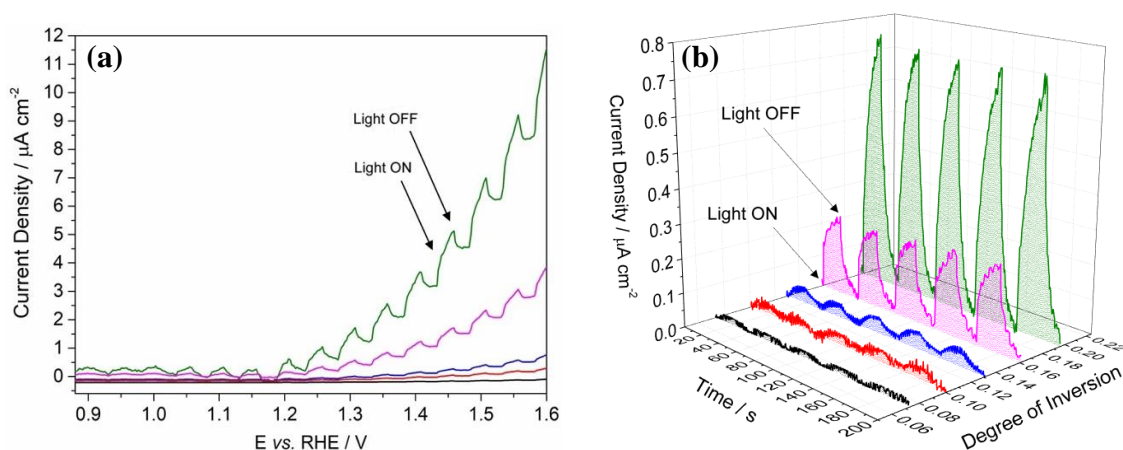


Figure 1. (a) Current density – voltage curves for the photoanodes made from ZFO pellets with different degrees of inversion. The measurements were performed in a 50% v/v methanol aqueous solution containing $0.1 \text{ mol L}^{-1} \text{ KNO}_3$ under chopped solar simulator irradiation (intensity output of 680 W m^{-2}). The light was turned on and off at 20 s intervals. (b) Chopped light chronoamperometry for the ZFO photoanodes measured with an externally applied bias of $+1.2 \text{ V vs. RHE}$. $x = 0.074$ (ZFO_773); $x = 0.104$ (ZFO_873); $x = 0.134$ (ZFO_973); $x = 0.159$ (ZFO_1073); and $x = 0.203$ (ZFO_1173).

Figure 2 shows the result of an incident photon-to-current efficiency (IPCE) measurement performed with the ZFO photoanode with a degree of inversion of $x \approx 0.20$ (ZFO_1173). This photoanode showed the highest photocurrent density for the methanol oxidation ($0.77 \mu\text{A cm}^{-2}$, Figure 1b). Considering the optical properties of the ZFO_1173 pellet reported previously [14], the absorbed photon-to-current efficiency (APCE) was calculated. It can be observed from Figure 2 that the APCE and, therefore, the ratio between the number of photogenerated holes reacting with methanol and the number of absorbed photons increased as the wavelength of the incident light became shorter. Thus, the photoanode converts the incident light into an electrical current more efficiently as the energy of the photons emitted by the excitation source increases.

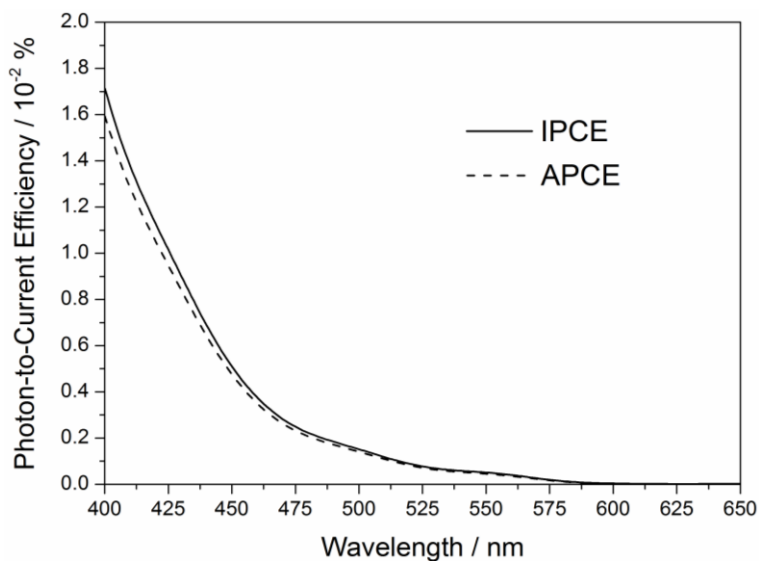


Figure 2. IPCE and APCE of the ZFO photoanode with $x \approx 0.20$ measured under an externally applied bias of +1.2 V vs. RHE in a 50% v/v methanol aqueous solution containing $0.1 \text{ mol L}^{-1} \text{ KNO}_3$. A monochromator was used for fine-tuning the wavelengths of the analyzing light to a final resolution of 1 nm.

Figure 3 shows the work function measured by the Kelvin probe technique for the ZFO pellet samples with different degrees of inversion. It was observed that the work function exhibited values ranging from 5.28 to 5.47 eV. Considering the experimental uncertainty ($\pm 0.13 \text{ eV}$), no significant changes in the Fermi level were observed as the degree of inversion of the ZFO pellets increased.

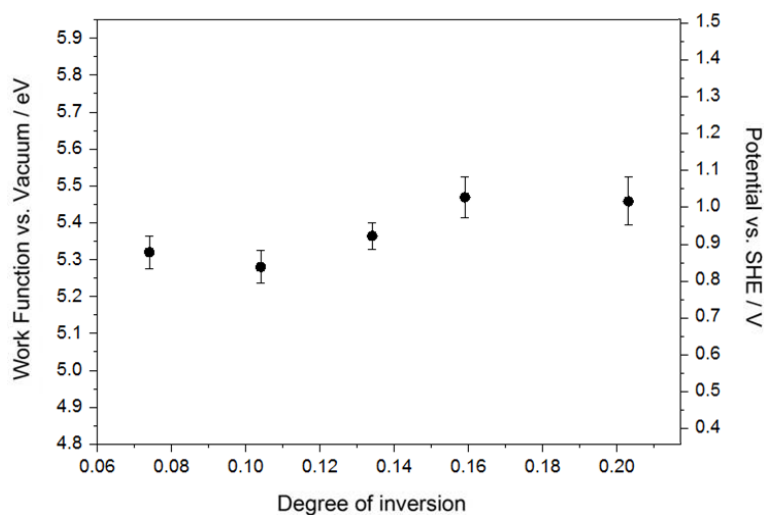


Figure 3. Work function of the ZFO pellet samples with degrees of inversion ranging from $x \approx 0.07$ to $x \approx 0.20$. The values were measured using a scanning Kelvin probe system. Before the measurement, the pellets were calcined at 673 K for 12 h to remove adsorbed water.

Time-averaged room-temperature photoluminescence measurements were carried out to investigate the effect of the degree of inversion on the electronic structure of ZFO. It becomes obvious from Figure 4 that all pellets exhibited three emission signals at approximately 464, 547, and 625 nm. The relative fluorescence quantum yield of the photoluminescence was determined by using quinine hemisulfate as a standard. Fluorescence quantum yields of 0.05% for the ZFO pellets with degrees of inversion of $x \approx 0.07$, $x \approx 0.10$, and $x \approx 0.13$, 0.04% for the pellet with $x \approx 0.15$, and 0.03% for the pellets with $x \approx 0.20$ were obtained.

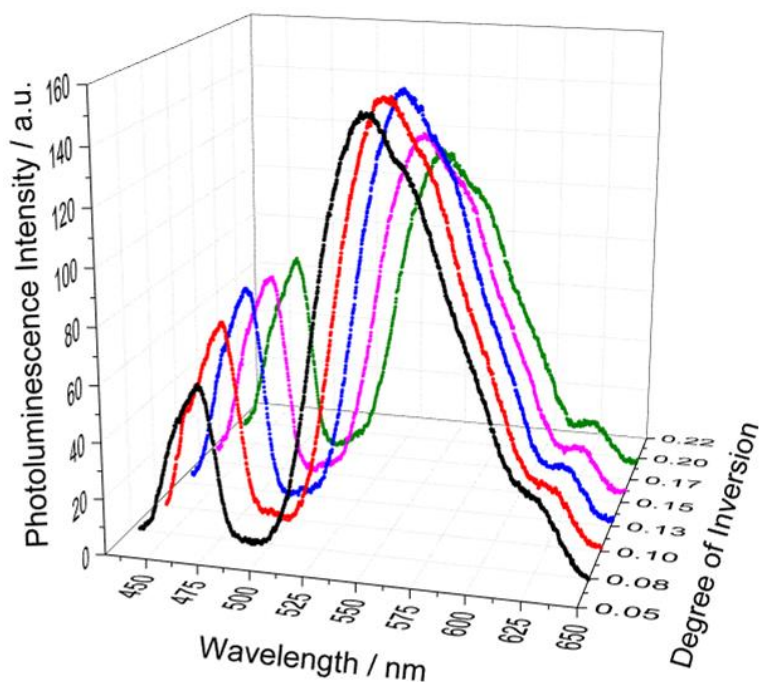


Figure 4. Time-averaged room-temperature photoluminescence of the ZFO pellets as a function of the degree of inversion. An excitation wavelength of 355 nm with an emission slit width of 10 nm was used for the measurement.

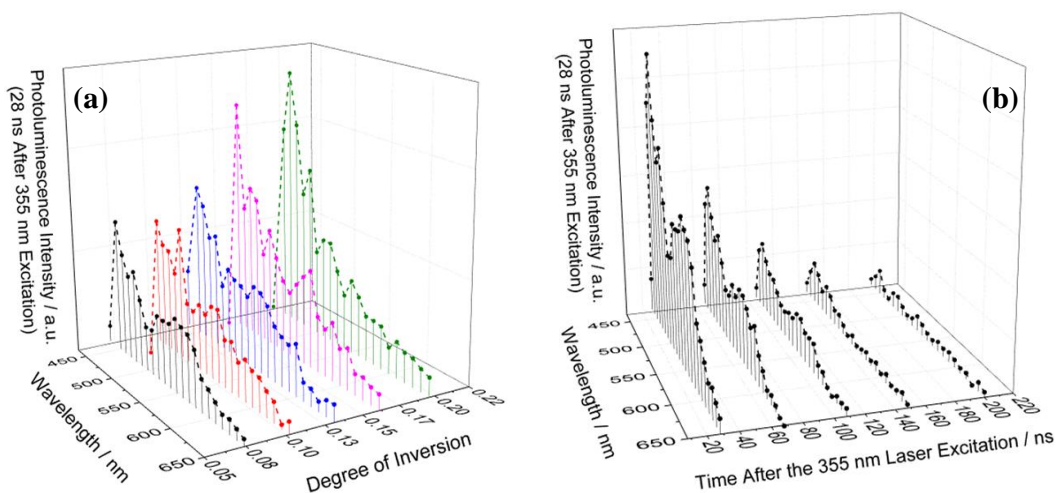


Figure 5. (a) Transient room-temperature photoluminescence spectra of the ZFO pellets as a function of the degree of inversion. The third harmonic (355 nm) of a Brilliant Nd:YAG laser with a pulse duration of 6 ns was used as the excitation source. The spectra were measured 28 ns after the excitation. $x = 0.074$ (ZFO_773); $x = 0.104$ (ZFO_873); $x = 0.134$ (ZFO_973); $x = 0.159$ (ZFO_1073); and $x = 0.203$ (ZFO_1173). (b) Transient room-temperature photoluminescence spectra of the ZFO pellet with $x = 0.074$ (ZFO_773) measured at different points in time after the 355 nm laser excitation.

Transient room-temperature photoluminescence measurements were conducted to study the lifetime of the electronic transitions. Figure 5a shows the photoluminescence spectra of the ZFO pellets with different degrees of inversion measured at 28 ns after the 355 nm laser excitation. Since 10 nm steps were used to record the transient signals, the spectral resolution was lower in comparison to the time-averaged measurements. Thus, the emission observed at approximately 625 nm in the time-averaged photoluminescence measurements (Figure 4) was not detected in the transient measurements. However, the emissions centered at 547 and 464 nm were clearly observed. The emission

centered at 464 nm showed a higher intensity than the emission centered at 547 nm. Figure 5b shows the room-temperature photoluminescence spectra of the ZFO pellet with a degree of inversion of $x \approx 0.07$ (ZFO_773) measured at different times after the laser excitation. The emission signal centered at 464 nm was weakly observed at 208 ns after the excitation, while the emission signal centered at 547 nm was no longer observed at 148 ns after the excitation.

3. Discussion

A series of ZFO photoanodes with different cation distributions between the tetrahedral and octahedral sites of the oxygen lattice were investigated to study the impact of the degree of inversion on the photoelectrochemical activity of ZFO. Due to the high-temperature calcination steps carried out during the preparation of the samples, large crystallite sizes of approximately 300 nm were obtained [14]. Large crystallite sizes imply large diffusion lengths for the photogenerated charge carriers [23,24]. Consequently, the charge carrier recombination rate increases and the photoelectrochemical efficiency of the material decreases [25]. Furthermore, low active surface areas are expected as the crystallite size increases [23,24]. Therefore, the large crystallite size of the ZFO photoanodes were responsible for the low photocurrent values obtained for the photoelectrochemical methanol oxidation (Figure 1). The large thickness of the films (approximately 750 μm) also had a negative impact on the photoelectrochemical activity for the same reasons above-mentioned. Higher photocurrent densities are reported in the literature for ZFO photoelectrodes [4,6,26,27]. In fact, the current benchmark in the performance of a partially reduced ZFO photoanode for solar water oxidation is 1.0 mA cm^{-2} at 1.23 V [8]. However, the aim of this work was to understand the impact of the degree of inversion on both the electronic properties and the photoelectrochemical activity of ZFO. The large particle size and thickness of the prepared ZFO electrodes as well as the absence of oxygen vacancies were the main reasons behind the observed low photocurrents. These drawbacks cannot be avoided when the synthesis of pristine ZFO samples in which the degree of inversion is the only independent variable is intended. However, although the measured photocurrents were below 1.0 $\mu\text{A cm}^{-2}$, an impact of the degree of inversion on the current density was clearly observed. It becomes obvious from Figure 1 that an increase of the cation distribution results in an increase in the photoelectrochemical activity of ZFO. The electrical conductivity of the pellets used in the present work was reported in a previous study [20]. An increase in the conductivity from 9.28×10^{-9} to 1.82×10^{-5} S cm^{-1} was observed as the degree of inversion increased from $x \approx 0.07$ to $x \approx 0.20$ [20]. Interestingly, a significant increase of two orders of magnitude was observed in the conductivity by increasing the degree of inversion from $x \approx 0.13$ to $x \approx 0.16$. This increase in the conductivity agreed with the large increase in the photocurrent from 0.05 to 0.24 $\mu\text{A cm}^{-2}$ that was observed for methanol oxidation as the degree of inversion increased from $x \approx 0.13$ to $x \approx 0.16$ (Figure 1b). It becomes evident from the preceding discussion that the increase in the electrical conductivity of the pellets with a higher degree of inversion is closely related to the improvement of the photoelectrochemical activity. However, the interrelation between the photoelectrochemical activity and the degree of inversion might also be related to other physicochemical properties of ZFO. Therefore, the impact of the cation distribution on the work function and the electronic transitions of ZFO was investigated.

As mentioned in the previous section, no significant changes in the work function were observed as the degree of inversion of the ZFO pellets increased. In a semiconductor, the work function represents the minimum energy required to remove an electron from the Fermi level into the free space [28]. The work function values obtained for the ZFO pellets corresponded, considering the IUPAC recommended value of -4.44 V for the absolute electrode potential of the hydrogen electrode [29], to Fermi levels around $+0.94$ V vs. SHE. Sun et al. [5] reported work function values ranging from 5.46 to 5.55 eV ($+1.02$ and $+1.11$ V vs. SHE) for mesoporous ZFO nanoparticles obtained via an evaporation-induced self-assembly method and calcined at different temperatures. The results were in good agreement with the values obtained in the present work. The work function of a semiconductor strongly depends on its doping level [30]. As well as for many n-type metal oxide semiconductors [31],

the mechanism for n-type doping of ZFO is the formation of oxygen vacancies [32], which results in the reduction of Fe^{3+} to Fe^{2+} [33]. As no Fe^{2+} was detected by Mössbauer spectroscopy for the ZFO pellets used in this work [14], a low donor density was expected. The high work function values obtained and the large anodic potential necessary for the methanol photoelectrochemical oxidation were the consequences of the low donor density. Furthermore, as similar work functions were observed for the different pellets, it was concluded that their donor densities were in the same order of magnitude and did not depend on the degree of inversion. For highly doped ZFO samples, work function values between 4.23 and 4.97 eV (−0.21 and +0.53 V vs. SHE) have been reported in the literature [27,34–36].

The optical band gap and the nature of the optical transitions of the pellets used for the present work were determined by measuring the diffuse reflectance and applying the derivation of absorption spectrum fitting (DASF) method, as was shown in a previous report [14]. Independent of the degree of inversion, the pellets exhibited an indirect band gap transition at approximately 614 nm (2.02 eV), and a direct band gap transition at approximately 532 nm (2.33 eV) [14]. These values were in good agreement with the 1.9 and 2.3 eV reported by Guijarro et al. [27] for the indirect and direct band gap, respectively. From density functional theory calculations, Yao et al. [37] showed that the valence band of ZFO consisted of $\text{O}^{2-} 2s$, $\text{Zn}^{2+} 3d$, $\text{Fe}^{3+} 3d$, and $\text{O}^{2-} 2p$ states. However, the valence band edge consisted of $\text{Fe}^{3+} 3d$ and mainly $\text{O}^{2-} 2p$ states [37]. The conduction band edge consisted of $\text{O}^{2-} 2p$ and mainly $\text{Fe}^{3+} 3d$ states [37]. At higher energies, the contribution from the $\text{Zn}^{2+} 4s$ states was observed in the density of states. Lv et al. [38] claimed that the energy band structures of ZFO were defined by considering the $\text{O}^{2-} 2p$ levels as the valence band edge and the $\text{Fe}^{3+} 3d$ levels as the conduction band edge. The emissions observed in Figure 4 at approximately 547 and 625 nm were in reasonable agreement with the direct and indirect band gap transitions at 532 and 614 nm, respectively [14]. Thus, these bands were ascribed to near-band-edge emissions due to the electron relaxation from $\text{Fe}^{3+} 3d$ levels located in the conduction band edge to $\text{O}^{2-} 2p$ levels in the valence band edge [39,40]. The emission centered at 464 nm might be related to transitions involving the Zn^{2+} cations [41,42]. It is well known for Fe-doped ZnO that the near-band-edge emission of ZnO centered at approximately 379 nm becomes red-shifted as the amount of Fe increases [42,43]. If the amount of Fe is high enough and spinel ZFO is formed as a secondary phase, a new emission centered at 464 nm is observed [42]. Therefore, the transition observed at approximately 464 nm could be ascribed to the electron relaxation from $\text{Zn}^{2+} 4s$ levels within the conduction band to $\text{O}^{2-} 2p$ in the valence band edge. This assignment agrees with the density of states presented by Yao et al. [37] Regardless of the nature of the electronic transitions, it is important to stress that the conduction band of ZFO does not exhibit a continuous density of empty electronic energetic states. Contradicting the semiconductor band theory [44], the conduction band of photoexcited electrons were delocalized in confined densities of states involving either $\text{Fe}^{3+} 3d$ levels or $\text{Zn}^{2+} 4s$ levels. Whether the photoexcited electron is delocalized in $\text{Fe}^{3+} 3d$ levels or $\text{Zn}^{2+} 4s$ levels depends on the energy of the excitation source. A scheme of the electronic excitation mechanism of ZFO is shown in Figure 6.

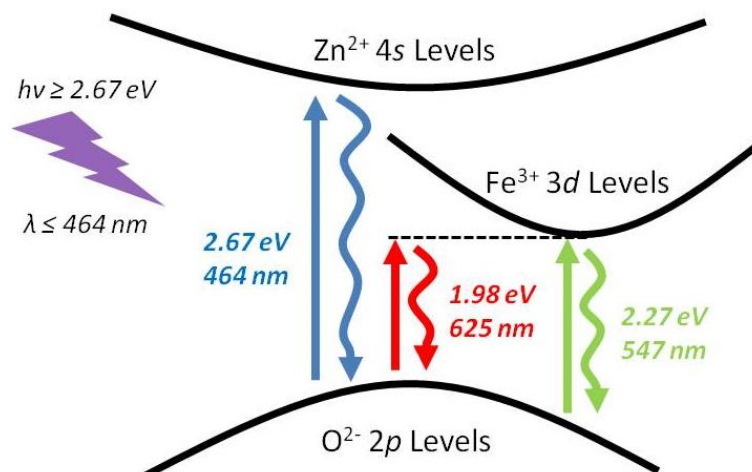


Figure 6. Scheme of the electronic transitions observed for ZFO when photons with wavelengths shorter than 464 nm (energy higher than 2.67 eV) are used for the excitation.

The influence of the $O^{2-} 2p$ to $Fe^{3+} 3d$ (indirect and direct) and the $O^{2-} 2p$ to $Zn^{2+} 4s$ electronic transitions on the photoelectrochemical efficiency of ZFO was deduced from the APCE measurement. According to Figure 2, when the ZFO photoanode is irradiated with light at wavelengths longer than 600 nm, the APCE is approximately zero. Thus, the methanol oxidation efficiency of the charge carriers generated via the indirect $O^{2-} 2p$ to $Fe^{3+} 3d$ transition (625 nm) is negligible. As also reported by Guijarro et al. [27], the indirect transition of ZFO does not effectively drive photoelectrochemical processes. The APCE increases as wavelengths ranging from 475 to 600 nm are used for the excitation of the photoanode. Under these irradiation conditions, the direct $O^{2-} 2p$ to $Fe^{3+} 3d$ transition occurs and the generated charge carriers can convert the incident light into an electrical current. Interestingly, a significant increase in the APCE values can be observed when the photoanode is irradiated with light at wavelengths shorter than 475 nm. This phenomenon could be attributed to two reasons. One is the increase in the absorptivity of the material as is observed from the diffuse reflectance measurements of the ZFO pellets reported elsewhere [14]. The second reason is the contribution of the charge carriers generated by the electronic transition from $O^{2-} 2p$ to $Zn^{2+} 4s$ levels (464 nm). The absorption coefficient of ZFO has approximately the same magnitude for wavelengths ranging from 400 to 500 nm [45,46]. Hence, the significant increase in the APCE should be observed at wavelengths longer than 475 nm if the larger light absorption of the material is responsible for this effect. Therefore, the increase in the APCE values at wavelengths shorter than 475 nm must be mainly due to the contribution to the methanol photooxidation of the charge carriers generated via the $O^{2-} 2p$ to $Zn^{2+} 4s$ electronic transition (464 nm).

The data presented in Figure 4 revealed that the degree of inversion affected the relative intensity of the room-temperature photoluminescence bands of ZFO. As the cation disorder increased, the intensity of the near-band-edge emission centered at 547 nm decreased, and the intensity of the emission centered at 464 nm increased. These emission bands were the result of electron-hole recombination processes and, thus, it is reasonable to assume that the observed increase or decrease in the emission intensity is due to an increase or decrease, respectively, in the number of generated electron-hole pairs. Therefore, as Zn^{2+} cations located in tetrahedral sites are interchanged by Fe^{3+} cations from octahedral sites, the probability of the electronic transition at 464 nm (from $O^{2-} 2p$ to $Zn^{2+} 4s$ levels) increases and the probability of the near-band-edge electronic transitions (from $O^{2-} 2p$ to $Fe^{3+} 3d$ levels) decreases. From the time-averaged photoluminescence measurements, it was observed that the intensity of the emission centered at 547 nm was higher than that of the emission centered at 464 nm (Figure 4). However, transient photoluminescence measurements showed a higher intensity for the emission centered at 464 nm (Figure 5a). This can be explained by a faster decay of the emission centered at 547 nm. In fact, the signal centered at 547 nm was no longer observed at 148 ns after the

excitation while the signal centered at 464 nm (due to the relaxation of the $O^{2-} 2p$ to $Zn^{2+} 4s$ electron excitation) was observed even 208 ns after the excitation (Figure 5b).

As discussed above, the electron-hole pairs generated by the electronic transitions observed at 547 and 464 nm are involved in the photoelectrochemical process occurring at the ZFO electrodes. It was shown that the transition centered at 464 nm had a higher efficiency for photoelectrochemical methanol oxidation than the transition centered at 547 nm (Figure 2). However, the valence band holes generated via both transitions had the same redox potential and, therefore, the same oxidizing activity. The higher efficiency of the transition centered at 464 nm was due to the longer lifetime of the generated charge carriers (Figure 5b). As the degree of inversion of the ZFO pellets increased, both, the amount of $O^{2-} 2p$ to $Zn^{2+} 4s$ electronic transitions and the photoelectrochemical activity increased.

4. Materials and Methods

Polycrystalline ZFO samples with degrees of inversion increasing from $x \approx 0.07$ to $x \approx 0.20$ were synthesized by means of a solid-state reaction as reported previously [14]. Briefly, stoichiometric amounts of ZnO (60 mmoles, Sigma Aldrich, Taufkirchen, Germany, $\geq 99.0\%$) and $\alpha\text{-Fe}_2\text{O}_3$ (60 mmoles, Sigma Aldrich, Taufkirchen, Germany, $\geq 99.0\%$) powders were ground in an agate mortar. The mixture was calcined in air at 1073 K for 12 h, cooled down to room temperature, and ground once again. Aliquots of 0.500 g were pressed into 13 mm diameter pellets applying a pressure of 55 MPa. The pellets were calcined at 1273 K for 2 h, cooled down to 1073 K and kept at this temperature for 12 h, then cooled down to 773 K and kept at this temperature for 50 h, and finally quenched in cold water. Some of the pellets (referred as ZFO_773) were separated and the rest were divided into four sets of pellets. These pellets were heated up with a rate of 300 K h^{-1} and calcined at 873, 973, 1073, and 1173 K for 25, 20, 12, and 10 h, respectively. As reported by O'Neill [12], these calcination times were sufficiently long for the ZFO pellets to reach a steady-state value of the degree of inversion. After this period of time, the calcined pellets were immediately quenched in cold water. These pellets are referred as ZFO_873, ZFO_973, ZFO_1073, and ZFO_1173. The ZFO pellets were sanded with Al_2O_3 sandpaper (KK114F, grit size P320, VSM Abrasives, Hannover, Germany) to a final thickness of $0.75 \text{ mm} \pm 0.02 \text{ mm}$.

Molecular nitrogen physisorption isotherms were measured at 77 K on a Quantachrome Autosorb-3MP instrument and argon physisorption isotherms were measured at 87 K on a Quantachrome Autosorb-1 instrument (3P Instruments GmbH & Co. KG, Odelzhausen, Germany). The pellets were outgassed in vacuum at 423 K for 24 h prior to the sorption measurements. Surface areas were estimated by applying the Brunauer–Emmett–Teller (BET) equation [47] and the total pore volumes were estimated by the single-point method at $p/p_0 = 0.95$.

Electrochemical and photoelectrochemical measurements were performed by employing a ZENNIUM Electrochemical Workstation (Zahner Scientific Instruments, Kronach, Germany) equipped with a three-electrode electrochemical cell with a Pt counter electrode and an Ag/AgCl/NaCl (3 mol kg^{-1}) reference electrode. ZFO working electrodes were prepared by attaching a copper wire with silver paint (Ferro GmbH, Frankfurt am Main, Germany) and conductive epoxy (Chemtronics, Kennesaw, GA, USA) to one face of the pellet sample. Photoelectrochemical measurements were performed in a 50% v/v methanol aqueous solution containing $0.1 \text{ mol L}^{-1} \text{ KNO}_3$. A solar simulator (LOT-Quantum Design GmbH, Darmstadt, Germany) consisting of a 300 W xenon-arc lamp provided with an AM 1.5-global filter was used as the irradiation source. An intensity output of 680 W m^{-2} at the position of the working electrode was measured using a SpectraRad Xpress spectral irradiance meter (B&W Tek, Newark, DE, USA). For the IPCE measurements, a TLS03 tunable light source (Zahner Scientific Instruments, Kronach, Germany) consisting of an array of monochromatic LEDs with emission wavelengths ranging from 400 to 650 nm was used. A monochromator was employed for fine tuning the wavelengths to a final resolution of 1 nm.

A scheme of the set-up used for the transient photoluminescence spectroscopy is shown in Figure 7. The third harmonic (355 nm) of a Brilliant Nd:YAG laser (Quantel, Lannion, France) with a pulse duration of 6 ns was used as the excitation source. A laser intensity of 3.0 mJ per pulse was

selected for the measurements. The intensity of the laser was measured using a Maestro laser power meter (Gentec-EO, Québec, Canada). The angle of the laser beam path was adjusted by rotating a Pellin-Broca prism beam steering module. The illumination area of the laser beam was approximately 0.5 cm^2 . The light emitted by the pellets after the laser excitation was collected by a Spectrosil lens and directed toward the monochromator by a folding mirror. The monochromator was connected with a PMT R928 photomultiplier detector (Hamamatsu Photonics, Hamamatsu, Japan). To avoid the overloading of the photomultiplier, a 370 nm cut off filter was introduced in front of the monochromator entrance. For the transient photoluminescence measurements, a constant voltage of 700 V was applied to the photomultiplier.

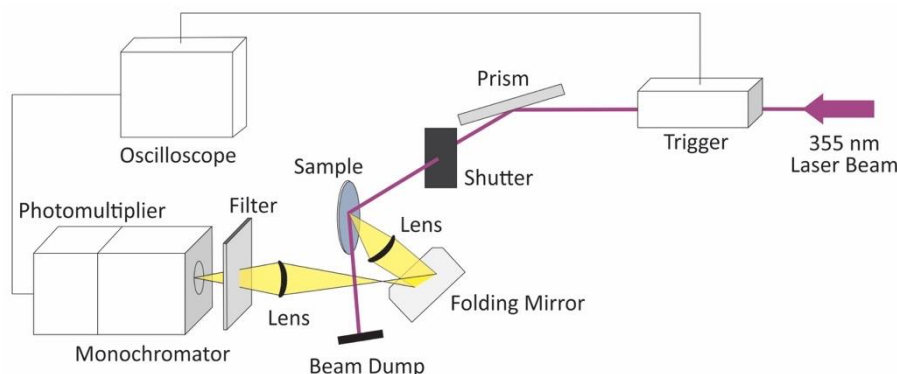


Figure 7. Scheme of the diffuse reflectance setup used for the transient photoluminescence measurements. The 355 nm laser excitation is shown in violet and the radiation emitted by the ZFO pellet is represented in yellow.

Time-averaged photoluminescence measurements were performed in an F-7100 fluorescence spectrophotometer (Hitachi, Tokyo, Japan). A wavelength of 355 nm was selected as the excitation source and the photoluminescence spectra were measured from 440 to 650 nm with a 240 nm min^{-1} scan rate. Excitation and emission slit widths of 10 nm were used. The relative fluorescence quantum yield was determined by employing a reported standard method [48–50]. Briefly, a $5 \times 10^{-3} \text{ mol L}^{-1}$ solution of quinine hemisulfate monohydrate ($\text{C}_{20}\text{H}_{24}\text{N}_2\text{O}_2 \cdot 0.5\text{H}_2\text{SO}_4 \cdot \text{H}_2\text{O}$, Sigma Aldrich, Taufkirchen, Germany, $\geq 98.0\%$) in 1 N H_2SO_4 , with an absolute quantum yield efficiency of 0.51 at 25°C [48], was used to determine the relative photoluminescence quantum yield of the ZFO pellets. For the time-averaged and the transient photoluminescence measurements, suspensions of the ZFO pellets were prepared. ZFO pellets were ground in an agate mortar and dispersed in deionized water by a one-hour ultrasound treatment (340 W L^{-1}). A concentration of 2.5 g L^{-1} was used for the measurements.

Work function measurements were performed with a scanning Kelvin probe system SKP5050 (KP Technology, Wick, Scotland) versus a gold reference probe electrode (probe area of 2 mm^2). The probe oscillation frequency was 74 Hz, and the backing potential was 7000 mV. Work function values were obtained by averaging 1000 data points for two different sites of each pellet. Prior to the measurements, the pellets were heated at 673 K for 12 h to remove adsorbed water. The cation diffusion process in ZFO is kinetically hindered at temperatures lower than 773 K [12]. Thus, the degree of inversion of the pellets did not change during the heat treatment.

5. Conclusions

The effect of the degree of inversion on the photoelectrochemical activity of ZFO was investigated. As the cation distribution changed from $x \approx 0.07$ to $x \approx 0.20$, the photoelectrochemical activity of ZFO increased. In order to study the correlation between this phenomenon and the electronic properties of the material, the work function as well as the time-averaged and transient photoluminescence of the different ZFO samples were studied. No significant effect of the degree of inversion on the Fermi level was observed. Regarding the photoluminescence results, the characteristic near-band-edge

emissions (547 and 625 nm for the direct and indirect transition, respectively) due to the electron-hole recombination involving $\text{Fe}^{3+} 3d$ and $\text{O}^{2-} 2p$ levels were observed. Furthermore, an emission of energy higher than the band gap was also detected. This emission was assigned to the relaxation of the excited state produced after the electronic transition from $\text{O}^{2-} 2p$ to $\text{Zn}^{2+} 4s$ levels (464 nm). Interestingly, the lifetime of the latter emission was observed to be longer than the lifetime of the near-band-edge emission. After excitation with photons with wavelengths shorter than 464 nm (blue and violet region of the visible light spectrum), electron-hole pairs were produced in ZFO by two apparently independent mechanisms (Figure 6). One pathway was the excitation of electrons from $\text{O}^{2-} 2p$ levels at the valence band maximum to $\text{Fe}^{3+} 3d$ levels at the conduction band minimum. The other was the excitation of electrons from $\text{O}^{2-} 2p$ levels at the valence band maximum to $\text{Zn}^{2+} 4s$ levels located within the conduction band. The charge carriers generated by the latter mechanism showed a longer lifetime and, consequently, a higher efficiency for the photoelectrochemical methanol oxidation. As the degree of inversion of ZFO increased, the transition involving the $\text{Zn}^{2+} 4s$ levels was favored, thus contributing to the observed increase in the photoelectrochemical activity.

Author Contributions: Conceptualization, L.I.G.; Investigation, L.I.G. and K.N.; Project administration, D.W.B.; Supervision, A.E., R.D., and D.W.B.; Writing—original draft, L.I.G.; Writing—review & editing, R.D.

Funding: This research was funded by the Deutsche Forschungsgemeinschaft (DFG) under the SPP 1613 program (BA 1137/22-1), the Niedersächsisches Ministerium für Wissenschaft und Kultur (NTH-research group “ElektroBak”), and the Korea government (MSIP) through NRF under the Global Research Laboratory program (2014K1A1A2041044).

Acknowledgments: The authors would like to thank Peter Behrens and Malte Schäfer (Institute for Inorganic Chemistry, Gottfried Wilhelm Leibniz University Hannover) for the physisorption measurements. The publication of this article was funded by the Open Access Fund of the Gottfried Wilhelm Leibniz Universität Hannover.

Conflicts of Interest: The authors declare no conflict of interest.

References

1. Dillert, R.; Taffa, D.H.; Wark, M.; Bredow, T.; Bahnemann, D.W. Research update: Photoelectrochemical water splitting and photocatalytic hydrogen production using ferrites (MFe_2O_4) under visible light irradiation. *APL Mater.* **2015**, *3*, 104001. [[CrossRef](#)]
2. Taffa, D.H.; Dillert, R.; Ulpe, A.C.; Bauerfeind, K.C.L.; Bredow, T.; Bahnemann, D.W.; Wark, M. Photoelectrochemical and theoretical investigations of spinel type ferrites ($\text{M}_x\text{Fe}_{3-x}\text{O}_4$) for water splitting: A mini-review. *J. Photonics Energy* **2016**, *7*, 12009. [[CrossRef](#)]
3. Chandrasekaran, S.; Bowen, C.; Zhang, P.; Li, Z.; Yuan, Q.; Ren, X.; Deng, L. Spinel photocatalysts for environmental remediation, hydrogen generation, CO_2 reduction and photoelectrochemical water splitting. *J. Mater. Chem. A* **2018**, *6*, 11078–11104. [[CrossRef](#)]
4. Kim, J.H.; Jang, Y.J.; Kim, J.H.; Jang, J.W.; Choi, S.H.; Lee, J.S. Defective ZnFe_2O_4 nanorods with oxygen vacancy for photoelectrochemical water splitting. *Nanoscale* **2015**, *7*, 19144–19151. [[CrossRef](#)]
5. Sun, M.; Chen, Y.; Tian, G.; Wu, A.; Yan, H.; Fu, H. Stable mesoporous ZnFe_2O_4 as an efficient electrocatalyst for hydrogen evolution reaction. *Electrochim. Acta* **2016**, *190*, 186–192. [[CrossRef](#)]
6. Hufnagel, A.G.; Peters, K.; Müller, A.; Scheu, C.; Fattakhova-Rohlfing, D.; Bein, T. Zinc ferrite photoanode nanomorphologies with favorable kinetics for water-splitting. *Adv. Funct. Mater.* **2016**, *26*, 4435–4443. [[CrossRef](#)]
7. Peeters, D.; Taffa, D.H.; Kerrigan, M.M.; Ney, A.; Jöns, N.; Rogalla, D.; Cwik, S.; Becker, H.W.; Grafen, M.; Ostendorf, A.; et al. Photoactive zinc ferrites fabricated via conventional CVD approach. *ACS Sustain. Chem. Eng.* **2017**, *5*, 2917–2926. [[CrossRef](#)]
8. Zhu, X.; Guijarro, N.; Liu, Y.; Schouwink, P.; Wells, R.A.; Le Formal, F.; Sun, S.; Gao, C.; Sivula, K. Spinel structural disorder influences solar-water-splitting performance of ZnFe_2O_4 nanorod photoanodes. *Adv. Mater.* **2018**, *30*, 1801612. [[CrossRef](#)] [[PubMed](#)]
9. Kirchberg, K.; Wang, S.; Wang, L.; Marschall, R. Mesoporous ZnFe_2O_4 photoanodes with template-tailored mesopores and temperature-dependent photocurrents. *ChemPhysChem* **2018**, *19*, 2313–2320. [[CrossRef](#)]

10. Kim, J.H.; Jang, Y.J.; Choi, S.H.; Lee, B.J.; Kim, J.H.; Park, Y.B.; Nam, C.M.; Kim, H.G.; Lee, J.S. A multitude of modifications strategy of ZnFe₂O₄ nanorod photoanodes for enhanced photoelectrochemical water splitting activity. *J. Mater. Chem. A* **2018**, *6*, 12693–12700. [[CrossRef](#)]
11. Guo, Y.; Zhang, N.; Wang, X.; Qian, Q.; Zhang, S.; Li, Z.; Zou, Z. A facile spray pyrolysis method to prepare Ti-doped ZnFe₂O₄ for boosting photoelectrochemical water splitting. *J. Mater. Chem. A* **2017**, *5*, 7571–7577. [[CrossRef](#)]
12. O'Neill, H.S.C. Temperature dependence of the cation distribution in zinc ferrite (ZnFe₂O₄) from powder XRD structural refinements. *Eur. J. Miner.* **1992**, *4*, 571–580. [[CrossRef](#)]
13. Pavese, A.; Levy, D.; Hoser, A.H. Cation distribution in synthetic zinc ferrite (Zn_{0.97}Fe_{2.02}O₄) from in situ high-temperature neutron powder diffraction. *Am. Mineral.* **2000**, *85*, 1497–1502. [[CrossRef](#)]
14. Granone, L.I.; Ulpe, A.C.; Robben, L.; Klimke, S.; Jahns, M.; Renz, F.; Gesing, T.M.; Bredow, T.; Dillert, R.; Bahnemann, D.W. Effect of the degree of inversion on optical properties of spinel ZnFe₂O₄. *Phys. Chem. Chem. Phys.* **2018**, *20*, 28267–28278. [[CrossRef](#)] [[PubMed](#)]
15. Bræstrup, F.; Hauback, B.C.; Hansen, K.K. Temperature dependence of the cation distribution in ZnFe₂O₄ measured with high temperature neutron diffraction. *J. Solid State Chem.* **2008**, *181*, 2364–2369. [[CrossRef](#)]
16. Akhtar, M.J.; Nadeem, M.; Javaid, S.; Atif, M. Cation distribution in nanocrystalline ZnFe₂O₄ investigated using x-ray absorption fine structure spectroscopy. *J. Phys. Condens. Matter* **2009**, *21*, 405303. [[CrossRef](#)] [[PubMed](#)]
17. Kumar, G.S.Y.; Naik, H.S.B.; Roy, A.S.; Harish, K.N.; Viswanath, R. Synthesis, optical and electrical properties of ZnFe₂O₄ nanocomposites. *Nanomater. Nanotechnol.* **2012**, *2*. [[CrossRef](#)]
18. Nakashima, S.; Fujita, K.; Tanaka, K.; Hirao, K.; Yamamoto, T.; Tanaka, I. First-principles XANES simulations of spinel zinc ferrite with a disordered cation distribution. *Phys. Rev. B* **2007**, *75*, 174443. [[CrossRef](#)]
19. Šepelák, V.; Tkáčová, K.; Boldyrev, V.V.; Wigmann, S.; Becker, K.D. Mechanically induced cation redistribution in ZnFe₂O₄ and its thermal stability. *Phys. B* **1997**, *234–236*, 617–619. [[CrossRef](#)]
20. Granone, L.I.; Dillert, R.; Heitjans, P.; Bahnemann, D.W. Effect of the degree of inversion on the electrical conductivity of spinel ZnFe₂O₄. *ChemistrySelect* **2019**, *4*, 1232–1239. [[CrossRef](#)]
21. Mitra, J.; Ghosh, M.; Bordia, R.K.; Sharma, A. Photoluminescent electrospun submicron fibers of hybrid organosiloxane and derived silica. *RSC Adv.* **2013**, *3*, 7591–7600. [[CrossRef](#)]
22. Vinosha, P.A.; Mely, L.A.; Jeronsia, J.E.; Krishnan, S.; Das, S.J. Synthesis and properties of spinel ZnFe₂O₄ nanoparticles by facile co-precipitation route. *Optik* **2017**, *134*, 99–108. [[CrossRef](#)]
23. Kočí, K.; Obalová, L.; Matějová, L.; Plachá, D.; Lacný, Z.; Jirkovský, J.; Šolcová, O. Effect of TiO₂ particle size on the photocatalytic reduction of CO₂. *Appl. Catal. B Environ.* **2009**, *89*, 494–502. [[CrossRef](#)]
24. Dodd, A.C.; McKinley, A.J.; Saunders, M.; Tsuzuki, T. Effect of particle size on the photocatalytic activity of nanoparticulate zinc oxide. *J. Nanoparticle Res.* **2006**, *8*, 43–51. [[CrossRef](#)]
25. Sivula, K.; Le Formal, F.; Grätzel, M. Solar water splitting: Progress using hematite (α-Fe₂O₃) photoelectrodes. *ChemSusChem* **2011**, *4*, 432–449. [[CrossRef](#)]
26. Kim, J.H.; Kim, J.H.; Jang, J.W.; Kim, J.Y.; Choi, S.H.; Magesh, G.; Lee, J.; Lee, J.S. Awakening solar water-splitting activity of ZnFe₂O₄ nanorods by hybrid microwave annealing. *Adv. Energy Mater.* **2015**, *5*, 1401933. [[CrossRef](#)]
27. Guijarro, N.; Bornoz, P.; Prévot, M.S.; Yu, X.; Zhu, X.; Johnson, M.; Jeanbourquin, X.A.; Le Formal, F.; Sivula, K. Evaluating spinel ferrites MFe₂O₄ (M = Cu, Mg, Zn) as photoanodes for solar water oxidation: Prospects and limitations. *Sustain. Energy Fuels* **2018**, *2*, 103–117. [[CrossRef](#)]
28. Kahn, A. Fermi level, work function and vacuum level. *Mater. Horizons* **2016**, *3*, 7–10. [[CrossRef](#)]
29. Trasatti, S. The absolute electrode potential: An explanatory note. *Pure Appl. Chem.* **1986**, *58*, 955. [[CrossRef](#)]
30. Matsumoto, Y. Energy positions of oxide semiconductors and photocatalysis with iron complex oxides. *J. Solid State Chem.* **1996**, *126*, 227–234. [[CrossRef](#)]
31. Raebiger, H.; Lany, S.; Zunger, A. Origins of the p-type nature and cation deficiency in Cu₂O and related materials. *Phys. Rev. B* **2007**, *76*, 45209. [[CrossRef](#)]
32. Nunome, T.; Irie, H.; Sakamoto, N.; Sakurai, O.; Shinozaki, K.; Suzuki, H.; Wakiya, N. Magnetic and photocatalytic properties of n- and p-type ZnFe₂O₄ particles synthesized using ultrasonic spray pyrolysis. *J. Ceram. Soc. Jpn.* **2013**, *121*, 26–30. [[CrossRef](#)]

33. Šutka, A.; Pärna, R.; Kleperis, J.; Käambre, T.; Pavlovska, I.; Korsaks, V.; Malnieks, K.; Grinberga, L.; Kisand, V. Photocatalytic activity of non-stoichiometric ZnFe_2O_4 under visible light irradiation. *Phys. Scr.* **2014**, *89*, 44011. [[CrossRef](#)]
34. Zheng, X.-L.; Dinh, C.T.; Pelayo García de Arquer, F.; Zhang, B.; Liu, M.; Voznyy, O.; Li, Y.-Y.; Knight, G.; Hoogland, S.; Lu, Z.-H.; et al. ZnFe_2O_4 leaves grown on TiO_2 trees enhance photoelectrochemical water splitting. *Small* **2016**, *12*, 3181–3188. [[CrossRef](#)]
35. Liu, X.; Zheng, H.; Li, Y.; Zhang, W. Factors on the separation of photogenerated charges and the charge dynamics in oxide/ ZnFe_2O_4 composites. *J. Mater. Chem. C* **2013**, *1*, 329–337. [[CrossRef](#)]
36. Nada, A.A.; Nasr, M.; Viter, R.; Miele, P.; Roualdes, S.; Bechelany, M. Mesoporous $\text{ZnFe}_2\text{O}_4@ \text{TiO}_2$ nanofibers prepared by electrospinning coupled to PECVD as highly performing photocatalytic materials. *J. Phys. Chem. C* **2017**, *121*, 24669–24677. [[CrossRef](#)]
37. Yao, J.; Li, X.; Li, Y.; Le, S. Density functional theory investigations on the structure and electronic properties of normal spinel ZnFe_2O_4 . *Integr. Ferroelectr.* **2013**, *145*, 17–23. [[CrossRef](#)]
38. Lv, H.; Ma, L.; Zeng, P.; Ke, D.; Peng, T. Synthesis of floriated ZnFe_2O_4 with porous nanorod structures and its photocatalytic hydrogen production under visible light. *J. Mater. Chem.* **2010**, *20*, 3665–3672. [[CrossRef](#)]
39. Lemine, O.M.; Bououdina, M.; Sajieddine, M.; Al-Saie, A.M.; Shafi, M.; Khatab, A.; Al-Hilali, M.; Henini, M. Synthesis, structural, magnetic and optical properties of nanocrystalline ZnFe_2O_4 . *Phys. B Condens. Matter* **2011**, *406*, 1989–1994. [[CrossRef](#)]
40. Zhu, X.; Zhang, F.; Wang, M.; Ding, J.; Sun, S.; Bao, J.; Gao, C. Facile synthesis, structure and visible light photocatalytic activity of recyclable $\text{ZnFe}_2\text{O}_4/\text{TiO}_2$. *Appl. Surf. Sci.* **2014**, *319*, 83–89. [[CrossRef](#)]
41. Fang, Z.; Wang, Y.; Xu, D.; Tan, Y.; Liu, X. Blue luminescent center in ZnO films deposited on silicon substrates. *Opt. Mater.* **2004**, *26*, 239–242. [[CrossRef](#)]
42. Srivastava, A.K.; Deepa, M.; Bahadur, N.; Goyat, M.S. Influence of Fe doping on nanostructures and photoluminescence of sol-gel derived ZnO. *Mater. Chem. Phys.* **2009**, *114*, 194–198. [[CrossRef](#)]
43. Chen, A.J.; Wu, X.M.; Sha, Z.D.; Zhuge, L.J.; Meng, Y.D. Structure and photoluminescence properties of Fe-doped ZnO thin films. *J. Phys. D. Appl. Phys.* **2006**, *39*, 4762–4765. [[CrossRef](#)]
44. Kittel, C. *Introduction to Solid State Physics*, 8th ed.; John Wiley & Sons: New York, NY, USA, 2005; ISBN 0-471-41526-X.
45. Sun, S.; Yang, X.; Zhang, Y.; Zhang, F.; Ding, J.; Bao, J.; Gao, C. Enhanced photocatalytic activity of sponge-like ZnFe_2O_4 synthesized by solution combustion method. *Prog. Nat. Sci. Mater. Int.* **2012**, *22*, 639–643. [[CrossRef](#)]
46. Xie, T.; Xu, L.; Liu, C.; Wang, Y. Magnetic composite $\text{ZnFe}_2\text{O}_4/\text{SrFe}_{12}\text{O}_{19}$: Preparation, characterization, and photocatalytic activity under visible light. *Appl. Surf. Sci.* **2013**, *273*, 684–691. [[CrossRef](#)]
47. Brunauer, S.; Emmett, P.H.; Teller, E. Adsorption of gases in multimolecular layers. *J. Am. Chem. Soc.* **1938**, *60*, 309–319. [[CrossRef](#)]
48. Melhuish, W.H. Quantum efficiencies of fluorescence of organic substances: Effect of solvent and concentration of the fluorescent solute. *J. Phys. Chem.* **1961**, *65*, 229–235. [[CrossRef](#)]
49. Fletcher, A.N. Quinine sulfate as a fluorescence quantum yield standard. *Photochem. Photobiol.* **1969**, *9*, 439–444. [[CrossRef](#)]
50. Würth, C.; Grabolle, M.; Pauli, J.; Spieles, M.; Resch-Genger, U. Relative and absolute determination of fluorescence quantum yields of transparent samples. *Nat. Protoc.* **2013**, *8*, 1535–1550. [[CrossRef](#)]

